Supporting Information:

Effect of hybrid field coupling in nanostructured surfaces on anisotropic signal detection in nanoscale infrared spectroscopic imaging methods

Ayona James,[†,‡] Maryam Ali,[†,‡] Zekai Ye,[‡] Phan Thi Yen Nhi,[†,‡] Sharon Xavi,[†,¶] Mashiat Huq,[¶] Sajib Barua,[¶,‡] Meng Luo,[¶] Yisak Tsegazab Gerase,[†,‡] Anna Elmanova,[†,‡] Robin Schneider,[‡] Olga Ustimenko,[§] Sarmiza-Elena Stanca,[‡] Marco Diegel,[‡] Andrea Dellith,[‡] Uwe Hübner,[‡] Christoph Krafft,[†,‡] Jasmin Finkelmeyer,[‡] Maximilian Hupfer,[†,‡] Kalina Peneva,[§,∥,⊥] Matthias Zeisberger,[‡] Christin David,[#,@] Martin Presselt,[†,‡] and Daniela Täuber[*,†,‡]

†*Institute of Physical Chemistry (IPC), Friedrich Schiller University Jena, 07743 Jena, Germany*

‡*Leibniz Institute of Photonic Technology (LIPHT), 07745 Jena, Germany*

¶*Abbe School of Photonics, Friedrich Schiller University Jena, 07745 Jena, Germany*

§*Institute of Organic and Macromolecular Chemistry (IOMC), Friedrich Schiller University Jena, 07743 Jena, Germany*

∥*Jena Center of Soft Matter (JCSM), Friedrich Schiller University Jena, 07743 Jena, Germany*

⊥*Center for Energy and Environmental Chemistry Jena (CEEC Jena), Friedrich Schiller University Jena, 07743 Jena, Germany*

#*Institute of Condensed Matter Theory and Solid State Optics (IFTO), Friedrich Schiller University Jena, 07743 Jena, Germany*

@*University of Applied Sciences Landshut, Landshut, Germany*

Abstract

The Supporting Information provides: (i) Exemplary BAM images of a PMIS-C8 film formed at the water surface before film deposition, (ii) of pristine Au substrates and PMIS-C8 monolayer films, (iii) topography images and PiF-contrasts of PiF-IR scan areas of the spectra presented in the main text together with two additional series of spectra on different sample positions, (iv) further PiF contrasts of PMIS-C8 monolayers on planar Au, and (v) further details on COMSOL modeling.

Brewster angle microscopy (BAM) of a PMIS-C8 monolayer

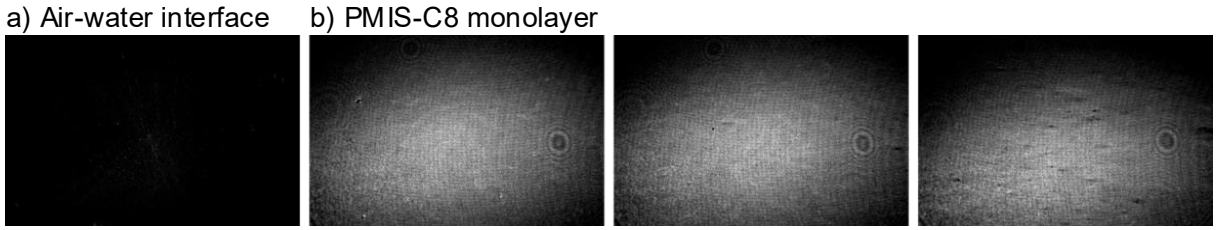

Figure S1: **BAM images acquired during PMIS-C8 monolayer deposition:** a) air-water interface before adding PMIS-C8 solution and b) three different positions of a PMIS-C8 monolayer formed on the water surface at a surface pressure $\Pi = 20$ mN/m.

The cleanliness of the air-water interface before the addition of the PMIS-C8 solution is confirmed by the almost completely dark BAM image (Figure S1a). At the final surface pressure of $\Pi = 20$ mN/m, PMIS-C8 forms a homogeneous film on top of the water surface; see (Figure S1b). Few areas show inhomogeneities, which appear as dark spots and lines, in particular, in the position shown in the rightmost image in Figure S1b.

AFM results of pristine substrates and PMIS-C8 monolayer films

Unless they are kept sealed or under cleanroom conditions, pristine Au surfaces are highly attractive for any kind of charged dust particles. AFM height images of all Au substrates and film samples show small heights in the range of 10 - 20 nm apart from larger dust particles. The higher resolution zoom image acquired on pristine planar Au shows up to 1 μm wide

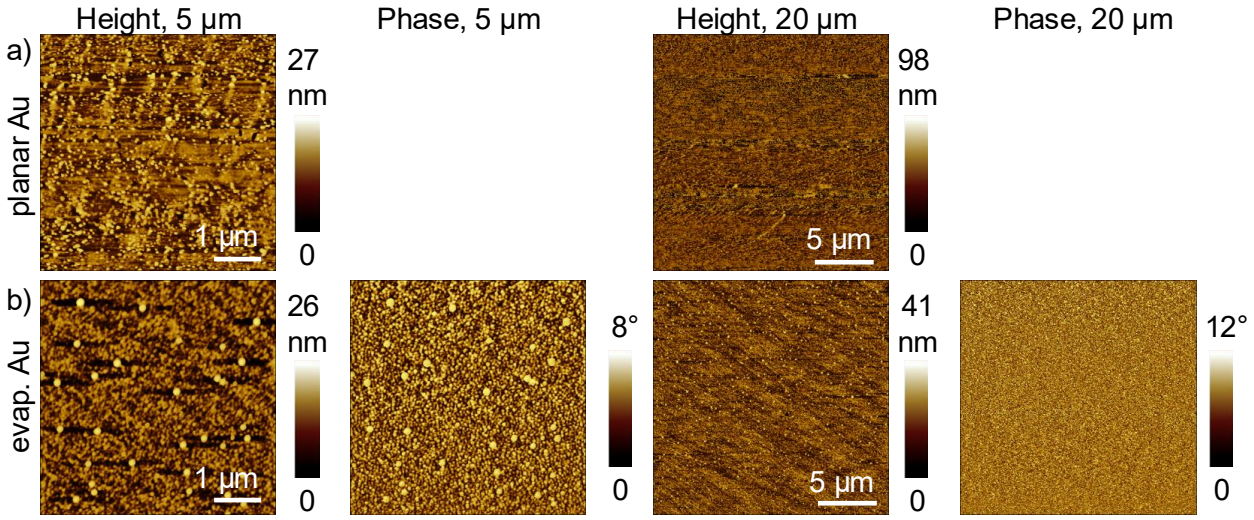

Figure S2: **AFM results on pristine Au substrates.** 5 μm zoom (left) and 20 μm overview regions (right): a) height images acquired on planar Au and b) height and corresponding phase images acquired on evaporated Au.

planar areas which are surrounded by small steps and some kind of debris (Figure S2a, left). In contrast, the surface of the pristine evaporated Au substrate is covered by the typical island structure showing an irregular pattern of islands $\approx$ 15 nm high and less than $\approx$ 100 nm wide, as can be seen in the higher resolution zoom and phase images in Figure S2b, left.

PMIS-C8 monolayers on planar Au show a pattern of up to several 100 nm wide planar flakes separated by small valleys and dips; see the higher resolution height images in Figures S3a and b, top row. In the corresponding phase images, the deeper dips are enveloped by increased phase angles (Figures S3a and b, upper middle row). The surface of the PMIS-C8 monolayers on nanostructured (evaporated) Au (Figure S3c and d, top row) follows the island structure seen on the pristine evaporated Au substrate (Figure S2b). However, the corresponding phase images of the two studied sample positions differ: apart from an $\approx$ 50 nm wide area in the top region, the phase image of position 2 shows an irregular pattern, which is absent in the phase image of position 1; compare Figures S3c and d, upper middle row. The larger scale overview phase image of the second position shows horizontal stripes; see Figure S3d, bottom row. In several cases, the pattern changes at positions

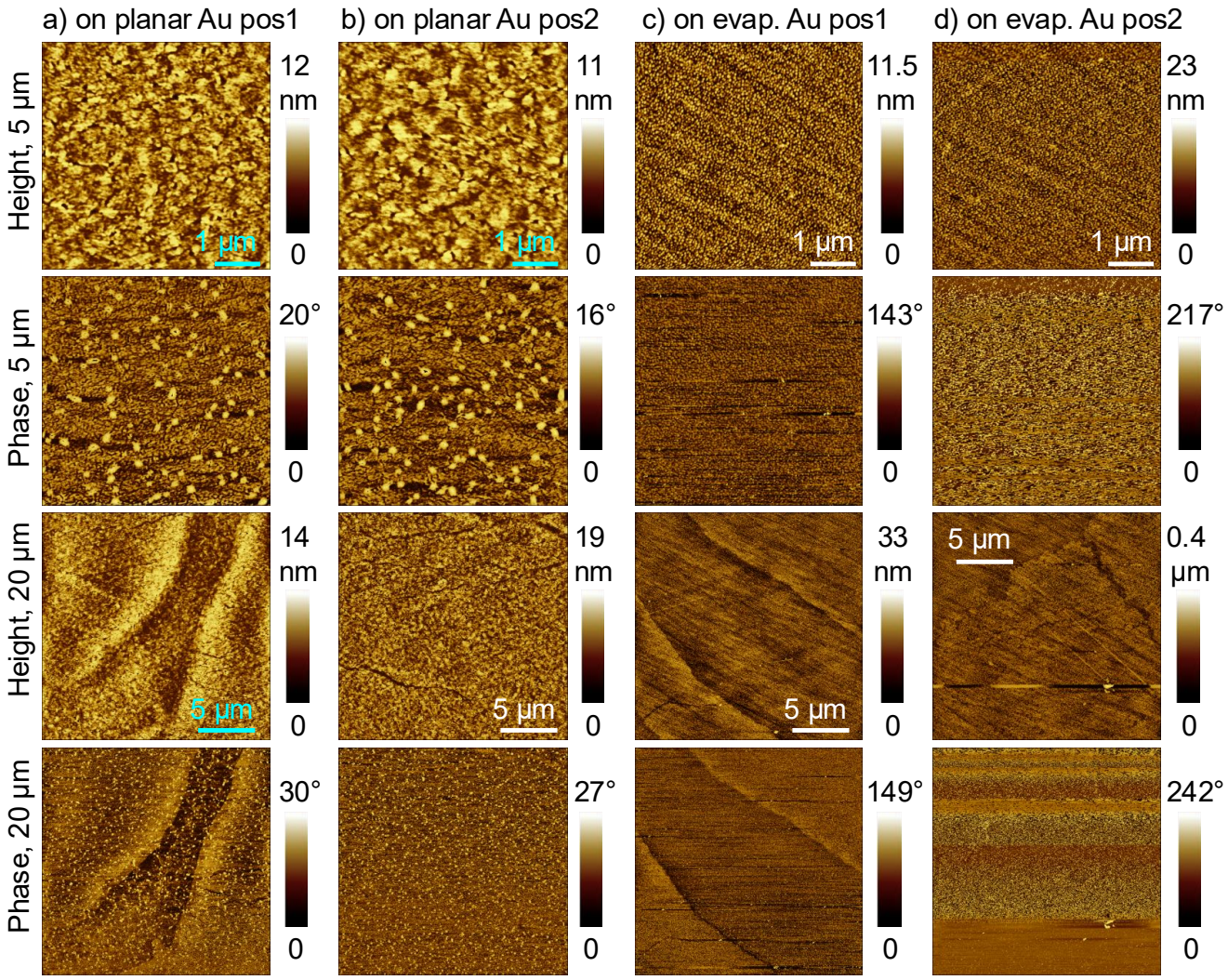

Figure S3: **AFM results on PMIS-C8 monolayer films.**

showing larger dust particles. We therefore assume that the pattern in the phase images was caused by dust particles moved over the sample by the tip during scanning. The larger scale height images of both monolayer films in Figure S3 (lower middle row) show thin cracks with variable orientation and length, which can be assigned to cracks in the monolayer films in agreement with inhomogeneities seen also in the BAM images of the film surfaces before its transfer to the substrates (Figure S1b).

Further details on PiF-IR spectra

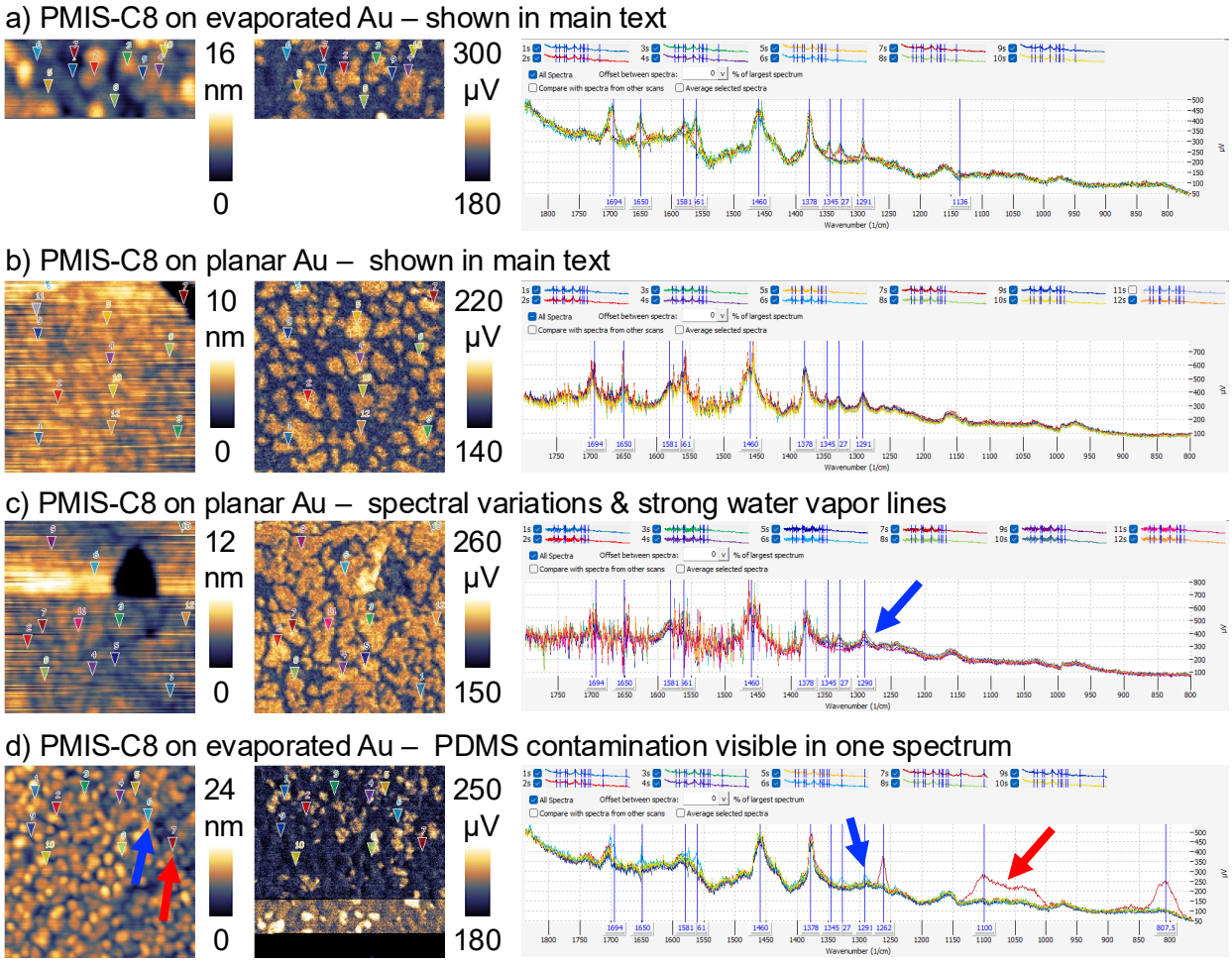

Figure S4: **Positions of PiF-IR point spectra.** AFM topography images (left column) and PiF contrasts (second column) of scans at $\nu = 1324$ cm^{-1} with positions of point spectra marked in matching colors for PMIS-C8 monolayers on a) nanostructured Au, b) on planar Au, c) on planar Au in a different sample position to b; the blue arrow in the corresponding plot of spectra marks intensity variation in the band at 1291 cm^{-1}, and d) on nanostructured Au in a different sample position to a; the blue arrow marks the position with higher intensity in the characteristic core vibration bands and red arrows mark contamination with PDMS.

PiF-IR spectra were acquired at several positions in previously scanned areas. Figure S4 shows AFM topography images (left column) and simultaneously acquired PiF contrasts at $\nu = 1324$ cm^{-1} (second left column) together with marked positions of point spectra. The right column shows the spectra in matching colors. The PiF contrasts of all sample positions show local variations in absorption at $\nu = 1324$ cm^{-1}. The positions of the PMIS-C8 spectra

on evaporated (nanostructured) Au discussed in the main text show a variety of low and high PiF intensities at 1324 cm^{-1} (Figure S4a). These spectra also show variations in the other absorption bands related to vibrations of the perylene core and imide group. In the two investigated sample positions of a PMIS-C8 monolayer on a planar Au substrate (Figures S4 b and c), positions showing high absorption at 1324 cm^{-1} were selected for acquisition of point spectra. Consequently, the perylene core and imide group absorption bands are visible in these spectra. Few spectra in sample c show lower intensity in these bands. This data set suffers from strong residual water vapor However, the variation can be seen in the two lower frequency absorption bands at 1324 and 1291 cm^{-1} (blue arrow). The other data set acquired on the PMIS-C8 monolayer on an evaporated Au substrate mainly contains spectra acquired at positions showing low PiF intensities at 1324 cm^{-1} (Figure S4d). Only one spectrum shows higher intensities in the characteristic absorption bands related to perylene core and imide group vibrations (blue arrows).

PiF-IR is highly sensitive to even small amounts of contamination.[S1] In our PiF-IR experiments, we frequently observed contributions of polydimethylsiloxane (PDMS), a highly volatile polymer that is used for storing AFM tips. PDMS could be easily discriminated in the data sets by its characteristic absorption bands at 1262 cm^{-1}, 1000-1150 cm^{-1} and 807 cm^{-1}. An example is shown and marked with red arrows in Figure S4d.

The bright and dark strips seen in the PiF contrast in (Figure S4d) result from instabilities in the control of the illuminating MirCat QCL. The QCL turned off during the scan and was turned on again after we noticed the issue. However, its intensity changed to a higher value when it was turned on again, causing the brighter area. After a while, it turned off again and was not turned on until the scan was complete.

PiF contrasts of PMIS-C8 monolayers on planar Au

To study PMIS-C8 monolayer formation and molecular arrangement on planar Au substrates, we scanned a 500 nm wide area of the film surface. The AFM topography image shows an

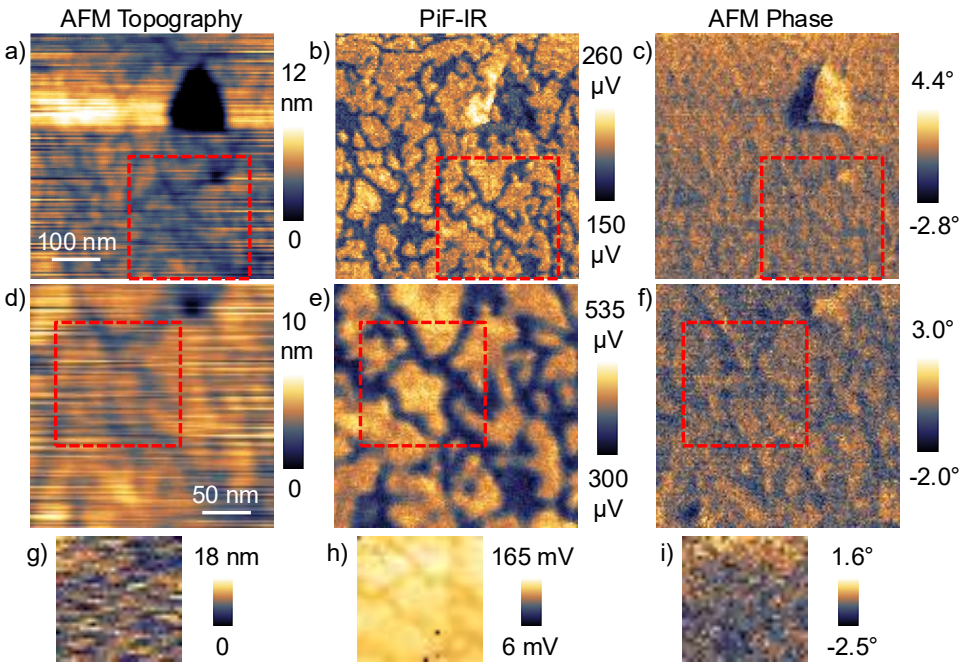

Figure S5: **PiF contrasts of PMIS-C8 monolayers on planar Au.** a-c) overview scan, d-f) higher resolution zoom in area marked by red boxes in the overview scan images and g-i) hyperspectral scan in positions marked by red boxes in higher resolution scan: a, d, g) AFM Topography; b and e) single frequency PiF contrasts acquired at $\nu = 1324$ cm^{-1} and $\nu = 1694$ cm^{-1}, respectively; c, f, i) simultaneously acquired phase images, and h) integrated PiF intensity over hyperscan spectral region.

irregular pattern containing up to 100 nm wide planar structures surrounded by irregularly shaped valleys; see Figure S5a. The scanned area also shows a deeper hole, in agreement with the larger area AFM images of PMIS-C8 monolayers on planar Au presented in Figure S3a and b. The topography image was processed using line-wise image correction to compensate for tilt from sample mounting (the same scan is presented together with acquired sepctra in Figure S4c). This resulted in an artifact showing bright stripes next to the hole. The PiF contrasts of the overview scan at $\nu = 1324$ cm^{-1} (Figure S5b) and the higher resolution zoom at $\nu = 1694$ cm^{-1} (Figure S5e) show higher values in the planar areas and lower signal in the valleys. This agrees with homogeneously oriented PMIS-C8 dimers in the planar areas. The integrated PiF contrast over the hyperscan (Figure S5h) shows less contrast between planar areas and valleys, which can be explained by the small total contribution of the characteristic bands of perylene core and imide group to the total PiF signal over the spectral range of

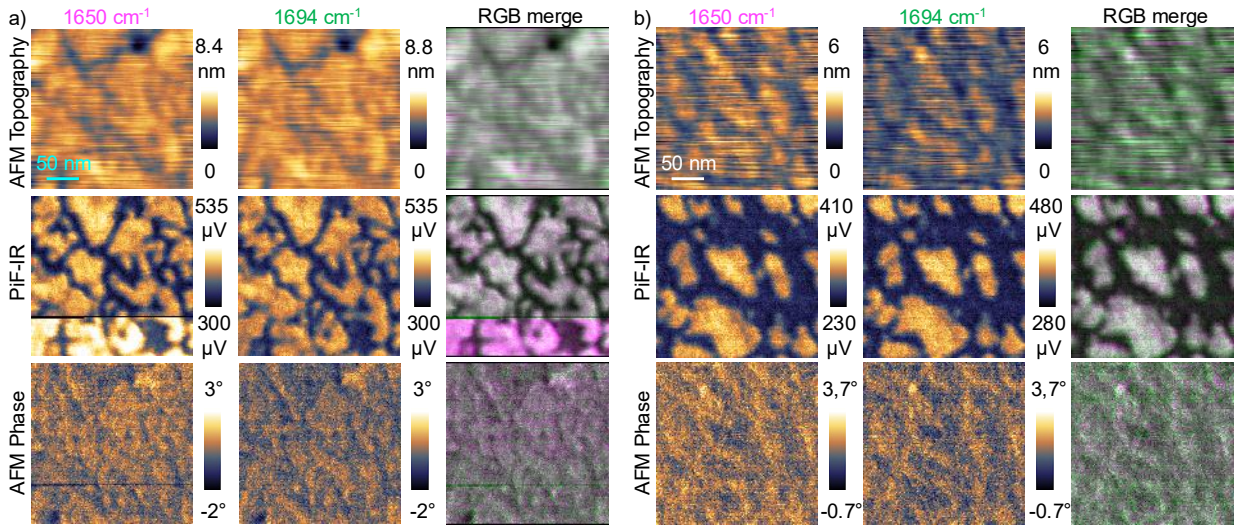

Figure S6: **Comparison of PiF contrasts of PMIS-C8 monolayers on planar Au in the two bands related to symmetric and asymmetric C=O stretch vibrations of the imide group.** AFM Topography images (top), PiF contrasts (middle) and simultaneously acquired phase images (bottom) acquired in two sample positions a) and b). Subsequent scans at $\nu = 1650$ cm^{-1} and $\nu = 1694$ cm^{-1} are presented as RGB merges with 1650 cm^{-1} (R+B = pink) and 1694 cm^{-1} (G).

1800 - 800 cm^{-1} covered by the hyperspectral scan.

To compare contributions of asymmetric and symmetric C=O stretch vibrations of the imide group, we acquired subsequent scans of the same sample position in two sample areas at the corresponding frequencies $\nu = 1694$ cm^{-1} and $\nu = 1650$ cm^{-1}, respectively. The two scans were cropped to the same sample area and presented as RGB merge images (with 1650 cm^{-1} (R+B = pink) and 1694 cm^{-1} (G)); see Figure S6. Due to the small hight difference and the homogeneous film material, the signal in the AFM height Figure S6 (top) and AFM phase images Figure S6 (bottom) is strongly influenced by instrument noise, resulting in horizontal stripes (fast scanning direction). During the scan at $\nu = 1650$ cm^{-1} on the first sample position Figure S6a, the MirCat QCL turned off and was manually turned on again. This resulted in a black horizontal line followed by a higher intensity in the bottom area of the scan. All PiF contrasts show high intensity in the planar sample areas and lower intensity in the surrounding valleys, as can be seen in Figure S6 (middle row). The RGB merges of the two PiF contrasts show small intensity variations for the scans at the two

different illumination frequencies. However, there is no distinct pattern. The variations are likely to be caused by instrument noise and a tiny offset between the pixel positions of the subsequent scans (scan resolution was 2 nm/pixel). The quite homogeneous PiF contrast in the two absorption bands agrees with the expected dimer formation of PMIS-C8 in monolayer films on metal substrates.[S2]

COMSOL modeling

We modeled the optical response of two different gold surfaces: (i) planar Au and (ii) nanostructured Au under plane-wave illumination, using the *Electromagnetic Waves, Frequency Domain* (EWFD) interface in COMSOL Multiphysics version 6.3 to study the plasmonic field of these surfaces for potential coupling with a metallic tip. All simulations were performed on a workstation with core processor Intel Core i7-14700KF CPU 3.40 GHz with installed RAM of 64 GB.

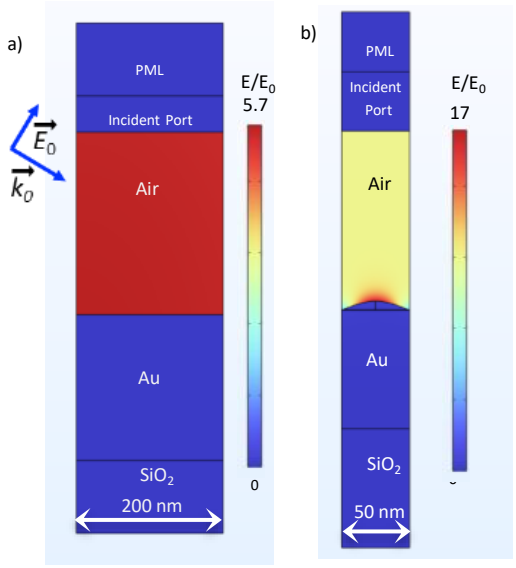

Figure S7: **Electric field coupling in the air-gold interface:** a) modeled planar Au substrate and b) modeled nanostructured Au substrate with incident electric field E_0 at 60° in the x-z-plane.

Refractive indices for Au and SiO_2 were taken from Olmon *et al.*,[S3] which is based on evaporated gold and measured in the region 0.300-24.93 μm, and Franta *et al.*,[S4] which is

valid in the spectral region 0.0248-125 μm, respectively. Both datasheets were imported from refractiveindex.com[S5] and the COMSOL interpolation feature was used. The region between the incident port and the gold surface is assumed to be air. The field strengths obtained for some characteristic vibration frequencies of PMIS-C8 obtained in both geometries are presented in Table S1. In the investigated spectral range of $\nu = 1291$ cm^{-1} to $\nu = 1819$ cm^{-1}, the field strengths on both planar and nanostructured Au surfaces are almost constant with a very small increase with increasing frequency. The ratio of field strengths for both geometries remains constant at 1.6.

Table S1: Simulated normalized photoinduced fields on nanostructured and planar Au.

ν (cm^{-1})	$E_{\text{nano-max}}$	$E_{\text{nano-av}}$	$E_{\text{planar-max}}$	$E_{\text{planar-av}}$	$E_{\text{nano-av}}/E_{\text{planar-av}}$
1291	16.91	5.73	6.95	3.55	1.61
1460	16.95	5.74	6.97	3.57	1.61
1557	16.93	5.76	6.97	3.58	1.61
1581	16.93	5.75	6.98	3.58	1.61
1650	16.94	5.77	6.98	3.56	1.62
1696	16.95	5.78	6.99	3.59	1.61
1750	16.97	5.79	6.99	3.60	1.61
1819	16.98	5.80	6.99	3.61	1.61
1850	16.99	5.80	7.00	3.61	1.61

The planar Au surface was modeled by placing a layer of 200 nm thick Au on 50 nm thick SiO_2 and $L = 200$ nm was used for the unit cell width; see Figure S7a. The nanostructured Au was modeled using a $\cos^2(\pi * x/R)$ function with a radius of $R = 25$ nm and a height of 15 nm and $L = 2R = 50$ nm was used for the unit cell width; see Figure S7b. This 2D parametric curve was then revolved around the z-axis to obtain a 3D nanostructure. The

nanostructure has a zero degree slope at its edge, which enables a smooth transition at the surface of the supporting 100 nm thick Au layer placed on a 100 nm thick SiO_2 substrate. A tetrahedral volume mesh with surface refinement is used for the Au substrate and is applied along with an extreme fine mesh of 2.5 nm average size on the surface of the nanostructure.

We used Floquet periodic boundary conditions applied to all four surrounding surfaces to simulate a periodic array of these nanostructures. The periodic port is excited with a TM polarized wave at an incidence of 60° with input port power of 1 W. PML layers are applied to the upper boundary to ensure absorption of reflected waves at this interface.

With these settings, we solve Maxwell's equations in the frequency domain using a fully coupled approach with the MUMPS direct solver at the frequency given via the wavelength through $f = \frac{c}{\lambda}$. Convergence tolerances of the calculations are below the COMSOL defaults of $\leq 10^{-3}$ relative. The normalized values of the electric field for both planar and nanostructured Au are given in the table S1 showing that there is an increase in the field coupling with the nanostructured Au.

References

(S1) Förster, M. W.; Otter, L. M.; Brocks, J. J.; Jayasoma, K.; Cisneros-Lazaro, D.; Nowak, D.; Stolarski, J.; Knowles, B. Quality Control Measures for Enhancing Confidence in Nanoscale IR Spectroscopy. *Geostandards and Geoanalytical Research* **2025**, *49*, 685–703, _eprint: https://onlinelibrary.wiley.com/doi/pdf/10.1111/ggr.70014.

(S2) Hupfer, M. L.; Meyer, R.; Deckert-Gaudig, T.; Ghosh, S.; Skabeev, A.; Peneva, K.; Deckert, V.; Dietzek, B.; Presselt, M. Supramolecular Reorientation During Deposition Onto Metal Surfaces of Quasi-Two-Dimensional Langmuir Monolayers Composed of Bifunctional Amphiphilic, Twisted Perylenes. *Langmuir* **2021**, *37*, 11018–11026, Publisher: American Chemical Society.

(S3) Olmon, R. L.; Slovick, B.; Johnson, T. W.; Shelton, D.; Oh, S.-H.; Boreman, G. D.;

Raschke, M. B. Optical dielectric function of gold. *Physical Review B* **2012**, *86*, 235147, Publisher: American Physical Society.

(S4) Franta, D.; Nečas, D.; Ohlídal, I.; Giglia, A. Optical characterization of SiO2 thin films using universal dispersion model over wide spectral range. Optical Micro-and Nanometrology VI. 2016; pp 253–267.

(S5) Polyanskiy, M. N. Refractive index database. 2025; `https://refractiveindex.info/`.